Physics and Chemistry of Minerals (2018) 45:641–654
https://doi.org/10.1007/s00269-018-0949-y

ORIGINAL PAPER

A first-principles and experimental study of helium diffusion in periclase MgO

Zhewen Song[1] · Henry Wu[1] · Shipeng Shu[1] · Mike Krawczynski[2] · James Van Orman[3] · Daniele J. Cherniak[4] · E. Bruce Watson[4] · Sujoy Mukhopadhyay[5] · Dane Morgan[1]

Received: 1 September 2017 / Accepted: 22 January 2018 / Published online: 13 February 2018
© Springer-Verlag GmbH Germany, part of Springer Nature 2018

Abstract
The distribution of He isotopes is used to trace heterogeneities in the Earth's mantle, and is particularly useful for constraining the length scale of heterogeneity due to the generally rapid diffusivity of helium. However, such an analysis is challenging because He diffusivities are largely unknown in lower mantle phases, which can influence the He profiles in regions that cycle through the lower mantle. With this motivation, we have used first-principles simulations based on density functional theory to study He diffusion in MgO, an important lower mantle phase. We first studied the case of interstitial helium diffusion in perfect MgO and found a migration barrier of 0.73 eV at zero pressure. Then we used the kinetic Monte Carlo method to study the case of substitutional He diffusion in MgO, where we assumed that He diffuses on the cation sublattice through cation vacancies. We also performed experiments on He diffusion at atmospheric pressure using ion implantation and nuclear reaction analysis in both as-received and Ga-doped samples. A comparison between the experimental and simulation results are shown. This work provides a foundation for further studies at high-pressure.

Keywords He diffusion · MgO · Ab initio · Diffusion mechanisms · Impurities

Introduction

Earth's mantle is unquestionably heterogeneous, and this heterogeneity has been observed over a wide range of length scales (vanderHilst et al. 1997). How the heterogeneous nature of the mantle relates to the isotopic signatures in basalts is of significant interest to geologists. Variations in basalt chemistry with respect to the abundance and isotopic composition of noble gases, and helium (He) in particular, have been used as proxies to trace mantle heterogeneity and structure, degassing and atmospheric formation, and mantle convection dynamics (Allegre et al. 1987).

Studies on He diffusivity to date have mostly focused on minerals important for thermochronology such as apatite, titanite, zircon and monazite as well as upper-most mantle materials including olivine (Cherniak and Watson 2012; Hart 1984) and pyroxenes (Trull and Kurz 1993). Recent experiments (Cherniak and Watson 2012) and simulations (Wang et al. 2015) reported the pressure effect on He diffusion in olivine up to 2.7 and 14 GPa, respectively. However, He behavior in the pure end member periclase MgO is of great importance for understanding He in the lower mantle, and has not previously been studied. This work, therefore, focuses on understanding the mechanisms and magnitudes of He diffusion in MgO.

Because He has no inherent charge, has an atomic radius intermediate between oxygen and magnesium, and is relatively compressible (Zhang et al. 2009), it is not obvious *a piori* how He interacts with interstitial sites, substitutional sites and diffusion mediating vacancies. It is useful

✉ Dane Morgan
ddmorgan@wisc.edu

[1] Department of Materials Science and Engineering, University of Wisconsin-Madison, Madison, WI 53706, USA

[2] Department of Earth and Planetary Sciences, Washington University in St. Louis, St. Louis, MO 63130, USA

[3] Department of Earth, Environment and Planetary Sciences, Case Western Reserve University, Cleveland, OH 44106, USA

[4] Department of Earth and Environment Sciences, Rensselaer Polytechnic Institute, Troy, NY 12180, USA

[5] Department of Earth and Planetary Science, University of California Davis, One Shields Avenue, Davis, CA 95616, USA

to review results of previous computational studies of He in other oxides and metals for guidance on where to focus our studies. Wang et al. (2015) studied the interstitial hopping of He in perfect olivine and obtained activation energies of up to 4.0 eV at zero pressure from first-principles calculations. Saadoune et al. (2009) simulated the incorporation and diffusion of He in both perfect and defect-bearing zircon ($ZrSiO_4$) and found that the available interstitial sites are energetically unfavorable and the interstitial mechanism is thus suppressed. Saadoune further pointed out that the presence of defect species in the zircon lattice changes the He solubility in the zircon lattice remarkably and indicated that these defects serve as a physical trap that suppresses the He diffusion. Dabrowski and Szuta (2013) obtained an interstitial He migration barrier of 4.15 and 3.95 eV in UO_2 and ThO_2, respectively. In contrast to oxides, He tends to diffuse interstitially in metals such as α-Fe, which was studied, e.g., by Fu and Willaime (2005). The interstitial mechanism is predicted to have a very low migration barrier (0.06 eV), while the migration of substitutional helium by the vacancy mechanism has a larger energy barrier of 1.1 eV. These studies suggest that both vacancy and interstitial mechanisms could have significant contributions to He diffusion.

In the present work, we utilized density functional theory (DFT) and kinetic Monte Carlo (KMC) simulations to investigate He diffusion in MgO, at different temperatures and different levels of impurity doping. We focus on as-received MgO and Ga^{3+}-doped MgO, where the latter doping was chosen to control the concentration of cation vacancies, which are created to balance the excess positive charge of the Ga. More specifically, we can potentially probe the diffusion mechanism through how it changes with vacancy content. We found that He diffusion is dominated by the interstitial mechanism at temperatures above 3000 K and by the vacancy-mediated mechanism at temperatures below 1500 K. Our model predicts reasonable upper and lower bounds for the He diffusivity that bracket our experimental data for a Ga-doped sample, but show a significant discrepancy compared to an as-received sample, possibly due to implantation damage effects. This work provides a foundation for further studies at high-pressure that can be used to directly assess behavior in the lower mantle.

Methodology

We constructed thermodynamic and kinetic models associated with He diffusion in MgO based on energetics calculated by DFT. As part of the diffusion model, we calculated all the energetics needed to qualitatively predict He solubility, therefore, we include an estimate of this value. Then we applied the transition state theory (Vineyard 1957) to model interstitial diffusion and a kinetic Monte Carlo model for the vacancy-mediated mechanism, and combined the two mechanisms for the total He diffusivity in MgO. In the following subsections, we describe the calculation methodologies in detail.

Density functional theory (DFT) calculations

The DFT calculations were performed with Vienna Ab Initio Simulation Package (VASP) (Kresse and Furthmuller 1996). The electron exchange and correlation potential was described by the general gradient approximation (GGA) with Perdew–Burke–Ernzerhof (PBE) exchange correlation functional. We used PAW (Blochl 1994) pseudopotentials with electronic configurations He ($1s^2$), Mg ($2s^2$), O (soft oxygen potential, denoted O_s by VASP, $2s^2\ 2p^4$).

Defect properties and migration barriers of interstitial and substitutional He in MgO were calculated for a $3\times3\times3$ (216 atom) supercells of the conventional rocksalt unit cell (8 atoms). We first fully relax the conventional perfect MgO cell (both volume and atomic coordinates) and obtain the lattice constant of 4.23 Å and then fix the volume to calculate the defected states and migration processes.

All the structural parameters were relaxed until the Hellmann–Feynman forces on each ion were less than 0.005 eV/Å. The plane-wave cut-off energy was set to 450 eV. A $4\times4\times4$ Monkhorst–Pack *k*-point mesh with a Gaussian smearing of 0.2 eV was used. Convergence tests with these settings suggest total energies are converged to within about 0.01 eV/atom for all the calculations.

Defects with formal charge will leave unbalanced electrons or holes in the calculation cell if proper compensating defects are not included. To mimic the compensation that would occur for such defects in the real systems we simply removed or added electrons. This approach allowed us to focus the calculations on the defect of interest without adding in complex and difficult to control defect–defect interactions. For example, the Mg vacancy leaves two holes somewhere in the cell if it is not compensated. Instead of adding two trivalent dopants into the cell for compensation, we remove the additional holes (i.e., add electrons) and balance the charge in the cell with a uniform background charge.

Migration barriers were calculated with the Climbing Image Nudged Elastic Band (CI-NEB) method (Henkelman et al. 2000). Phonon frequency calculations were performed by determining the Hessian matrix (matrix of the second derivatives of the energy with respect to the atomic positions) by finite differences method considering only the frequencies for the hopping atom, i.e., the hopping atom is displaced in the direction of each Cartesian coordinate and from the forces the Hessian matrix is determined. Imaginary frequency will appear along a certain direction in the saddle point configuration and the phonon attempt frequency can be determined by the Vineyard theory (Vineyard 1957). All the

migration barriers and phonon calculations were automated with the materials simulation toolkit (MAST) (Mayeshiba et al. 2017).

Formalism for solubility of He

Although He solubility plays no role in our diffusion model, we have all the energies necessary for a qualitative estimate of its solubility in MgO under difference conditions. As this quantity could be of value to future researchers, we provide the information in addition to our diffusion analysis. This section gives the formalism for determining He solubility. To model the He solubility, first we consider the relative amounts of substitutional and interstitial He, and then we consider the amount of interstitial He in equilibrium with He gas.

The DFT total energy calculations find only one local minimum each for the He cation substitutional and interstitial sites (see Fig. 1). The substitutional He is centered on the site of the substituted Mg, and the stable interstitial He site is the tetrahedral site of the face-centered cubic sublattice of Mg. Different interstitial sites were explored and the stable site was perturbed by random displacement in x, y, and z directions of about 0.1 Å to look for other local minima, but only one stable interstitial site was obtained. At thermodynamic equilibrium, assuming dilute defects without interactions, the exchange of substitutional with interstitial and vacancy produces the relationship:

$$\frac{c_{\text{sub}}}{c_{\text{int}} c_V} = \exp\left(-\frac{\Delta G_{\text{vac-int}}}{kT}\right) \tag{1}$$

where c_{sub}, c_{int}, and c_V denotes the concentration of the substitutional He, interstitial He, and vacancy, respectively, and $\Delta G_{\text{vac- int}}$ is the binding non-configurational Gibbs free energy of He trapped by the vacancy from the interstitial site, given by

$$\Delta G_{\text{vac- int}} = (G_{\text{sub}} + G_{\text{perfect}}) - (G_{\text{int}} + G_V) \tag{2}$$

Here G_X are non-configurational Gibbs free energies for the system in structure X. Note that X = sub, perfect, int, V refer to an MgO structure with substitutional He on the Mg site, perfect MgO without He, perfect MgO with an interstitial He, and a single Mg vacancy in MgO with no He, respectively.

The non-configurational Gibbs free energy of the solid can be defined as

$$G_{\text{solid}} = E_{\text{solid}} + G_{\text{vib}} + G_{\text{non-vib}} + PV_{\text{solid}} \tag{3}$$

where E_{solid} is the lattice energy from DFT calculation, G_{vib} is the free energy due to vibrational degrees of freedom, $G_{\text{non-vib}}$ is the free energy due to degrees of freedom that are not vibrational or configurational, P is external pressure and V_{solid} is volume. At zero pressure (or one atmosphere pressure) the PV_{solid} term is negligible. The $G_{\text{non-vib}}$ term is assumed to cancel in the Gibbs free energy differences in Eq. (3) so we will not calculate it. As the only major non-vibrational and non-configurational contributions are expected to be electronic, the fact that this system is a non-magnetic insulator with a large band gap means that the changes in $G_{\text{non-vib}}$ are expected to be negligible. Similarly, we will assume all vibrational terms cancel and not model them, except for those associated with He, which will be included in the solid phase as the corresponding degrees of freedom will be included in the gas phase. We model He solid phase vibrations with the Einstein vibrational model, which yields the following expression for the He vibrational Gibbs free energy (Callaway 1974).

$$G_{\text{He}}^{\text{vib}}(T) = \sum_{i=1}^{3} kT \ln\left[2\sinh\left(\frac{\hbar\nu_i}{2kT}\right)\right] \tag{4}$$

where the ν_i are the vibrational frequencies of the He. We note that this simple model for He vibrational free energy could have significant absolute errors that will not be cancelled by corresponding errors in the gas phase thermodynamics. Errors of $\approx kT$ lead to errors of ≈ 3 in the absolute solubility, which, therefore, should only

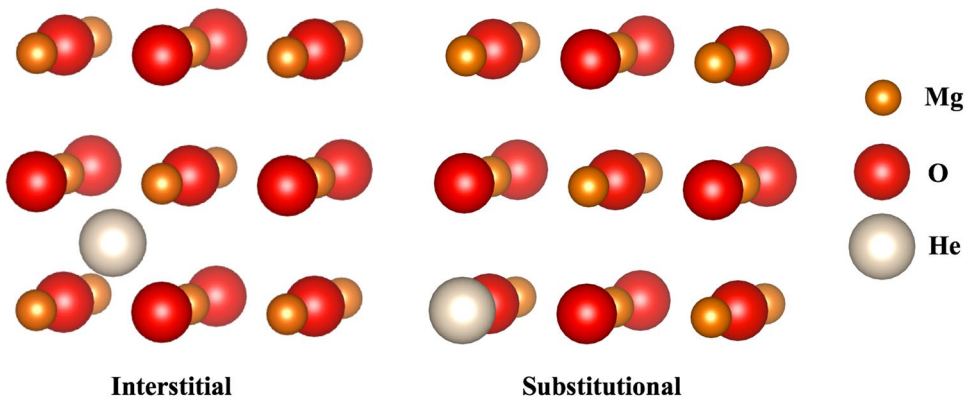

Fig. 1 Local minimum configuration for He interstitial and substitutional sites

be used for order of magnitude estimates. However, the solubility values are not of direct relevant for this work and are included only for the reader's convenience, so a more accurate approach is not considered. Using the DFT approaches described in "Density functional theory (DFT) calculations", the He binding energy is found to be $(E_{\text{sub}} + E_{\text{perfect}}) - (E_{\text{int}} + E_{\text{V}}) = -2.44$ eV. This value is calculated using a $3\times3\times3$ supercell and is within ~0.01 eV compared to a $4\times4\times4$ supercell, which suggests that this binding energy has converged in the $3\times3\times3$ cell. However, we will see later in "He–vacancy binding energetics" that the vacancy–impurity binding energetics, including vacancy-X (X = Al, Ga, ...), vacancy–vacancy and vacancy–He (both substitutional) are rather sensitive to the supercell size.

To obtain the interstitial He concentration in equilibrium with a gas we assume the interstitials He is dilute and use the relation

$$c_{\text{int}} = \exp\left(-\frac{\Delta G_{\text{int-perfect}}}{kT}\right) \tag{5}$$

where $\Delta G_{\text{int-perfect}}$ is the free energy differences between the products (interstitial He) and reactants (perfect MgO and helium gas):

$$\Delta G_{\text{int-perfect}} = G_{\text{int}} - (G_{\text{perfect}} + \mu_{\text{He}}) \tag{6}$$

Here μ_{He} is the He chemical potential, which can be approximated as

$$\mu_{\text{He}} = E_{\text{He}}^{\text{VASP}} + \Delta H_{\text{He}}(T, P^0) - \frac{5}{2}kT^0 - TS_{\text{He}}(T, P^0) + kT\ln\left(\frac{P}{P^0}\right) \tag{7}$$

where P is the He gas partial pressure, $E_{\text{He}}^{\text{VASP}}$ is the $T=0$ K energy as found in the DFT calculations, $\Delta H_{\text{He}}(T, P^0)$ is the enthalpy of He gas relative to the gas at standard pressure and temperature (T^0, P^0), and $S_{\text{He}}(T, P^0)$ is the He gas entropy at temperature T and pressure P^0. The $-\frac{5}{2}kT^0$ term shifts the reference state from the enthalpy of the gas at standard pressure and temperature to the internal energy of the gas at zero temperature (it includes a term for kinetic energy of $-\frac{3}{2}kT^0$ and the PV term of $-kT^0$) and the $E_{\text{He}}^{\text{VASP}}$ then shifts the reference state to the He pseudoatom energy used in VASP, making the chemical potential reference appropriate for comparison to other VASP calculated energies. The experimentally determined enthalpy and entropy terms for He gas can be found in (Weast 1988). Combining Eqs. (1)–(7) allows us to solve for the He concentration in interstitial and substitutional sites, and therefore, the overall He solubility, as a function of temperature and He partial pressure.

Free and bound extrinsic cation vacancy concentration

We assume that in MgO all vacancies are produced by cation dopants with valence greater than 2+ and that the concentrations of the vacancies are determined exactly by charge balance requirements. This assumption is a good approximation as thermally produced vacancies in MgO are generally very low in concentration. However, not all impurity-induced vacancies are available to mediate diffusion on the cation sublattice as vacancies and dopants can interact to form a bound complex, potentially trapping the vacancy. In this work, we follow the general approach of (Perkins and Rapp 1973; Van Orman et al. 2009) and assume that such complexes consist of vacancy–dopant pairs and dopant–vacancy–dopant three-body complexes. It is often assumed that the complexes are immobile enough that vacancies bound into complexes are unavailable to significantly mediate He transport. However, this is an assumption that needs further study, although such study is beyond the scope of this work. In this work, we will simply explore two limiting cases, in particular, one case where vacancies are assumed to be fully available for He transport, and the other case where vacancies in complexes are assumed to be totally immobile and unavailable for He transport.

The concentration of vacancy complexes can be determined by the complex binding equation

$$\begin{cases} \text{A} + \text{V} \rightleftharpoons \text{AV} \\ 2\text{A} + \text{V} \rightleftharpoons \text{AVA} \end{cases} \tag{8}$$

where A is a trivalent dopant on Mg sublattice, V is the cation vacancy, AV is the impurity–vacancy pair, and AVA is the three-body complex.

To obtain the free-vacancy concentration c_V^f with a single trivalent impurity species A, we set up the system of equations below following the conservation of different species and equilibrium conditions:

$$\begin{cases} c_{\text{V}}^f + c_{\text{AV}} + c_{\text{AVA}} = c_V = \frac{1}{2}c_{\text{A}} \\ c_{\text{A}}^f + c_{\text{AV}} + 2c_{\text{AVA}} = c_{\text{A}} \\ \frac{c_{\text{AV}}}{c_{\text{A}}^f c_{\text{V}}^f} = Z_2 \exp\left(-\frac{G_2^b}{kT}\right) \\ \frac{c_{\text{AVA}}}{\left(c_{\text{A}}^f\right)^2 c_{\text{V}}^f} = Z_3 \exp\left(-\frac{G_3^b}{kT}\right) \end{cases} \tag{9}$$

where the superscript f denotes the free or unbound species, subscript AV and AVA denote the bound vacancies, which are the vacancy–impurity pair and the three-body complex, respectively. All concentrations are measured per cation lattice site. The factor 1/2 in the first equation comes from the charge neutrality constraint for trivalent impurities and

would be altered for other formal charges on the impurity. $Z_2 = 12$ and $Z_3 = 6$ are the number of distinguishable orientations of the pair and the three-body complex (Perkins and Rapp 1973), respectively. G_2^b and G_3^b are the free energy of association, or binding energy, of the pair and the three-body complex, respectively.

He–vacancy binding energetics

It is necessary to determine the binding energies for He–vacancy (we use this notation to refer to a He substituting on a Mg site binding to a nearby vacancy) and vacancy–vacancy as they play a critical role in the prediction of vacancy-mediated He diffusion. Binding energy can be expressed as the difference of the energy of the complex referenced to the energies of the isolated species. The binding energies of He–vacancy and vacancy–vacancy can be written respectively as

$$E^B_{\text{He-vac}} = E_{\text{He-vac}} + E_{\text{perfect}} - E_{\text{He}} - E_{\text{vac}} \tag{10.1}$$

$$E^B_{\text{vac-vac}} = E_{\text{vac-vac}} + E_{\text{perfect}} - 2E_{\text{vac}} \tag{10.2}$$

Because we used periodic boundary conditions in the simulations, the charged defects interact with their images through long-range electrostatic Coulomb potentials. Following (Leslie and Gillan 1985), a first-order correction was applied to our calculations as

$$\Delta E_{\text{LG}} = \frac{q^2\alpha}{8\pi L\varepsilon_0\varepsilon} \tag{11}$$

where q is the charge of the system, α is the Madelung constant, L is the size of the supercell, and ε_0 and ε are the permittivity in vacuum and bulk, respectively. DFT calculations give a value of ε to be 9.84, which is consistent with literature values such as (Ammann et al. 2012). In this work, no attempt is made to model He–vacancy binding free energies, and only the DFT energies are used.

Diffusivity formalism

All the diffusion coefficients we calculate in this paper are atomic tracer diffusion coefficients, which can be generally described by the transition state theory (Vineyard 1957). For He diffusion in Mg by the interstitial mechanism, we have the diffusivity

$$D_{\text{int}} = \frac{Z_I}{6}\left(\frac{a}{2}\right)^2 \nu^* e^{-\frac{H_{\text{int}}}{kT}} = D^0_{\text{int}} e^{-\frac{H_{\text{int}}}{kT}} \tag{12}$$

where $Z_I = 6$ in the interstitial mechanism, a is the lattice parameter for MgO, H_{int} is the migration enthalpy barrier, which can be approximated as an energy calculated at fixed volume and determined using the CI-NEB, ν^* is the attempt frequency from Vineyard theory (Vineyard 1957), i.e., $\nu^* = \frac{\prod_{i=1}^{3N}\nu_i}{\prod_{i=1}^{3N-1}\nu_i'}$ (N = number of atoms involved in the migration, ν_i and ν_i' are the stable phonon frequencies in the initial and activated state, respectively), and D^0_{int} is a prefactor for diffusion that contains the factors not related to migration enthalpy. In this work, we will include only phonon frequencies of the migrating atom in calculating the attempt frequencies ν^*. This is equivalent to the Einstein approximation used in Eq. (4) for the initial and activated state. To justify this approach, we note that this approximation was explored in detail in a study of substitutional impurity diffusion in metals, where it gave errors of only about 2–4× (Wu et al. 2016). The vacancy-mediated diffusivity is determined by kinetic Monte Carlo and discussed in "The kinetic Monte Carlo model".

The overall He diffusivity can finally be approximated as the combination of interstitial and vacancy-mediated diffusivities weighted by the corresponding species concentration, namely

$$D_{\text{tot}} = \frac{C_{\text{int}}D_{\text{int}} + C_{\text{sub}}D_{\text{sub}}}{C_{\text{int}} + C_{\text{sub}}} = \frac{D_{\text{int}} + \gamma D_{\text{sub}}}{1+\gamma} \tag{13}$$

where C_{int} is the interstitial He concentration, C_{sub} is the substitutional He concentration on Mg sites and $\gamma = \frac{C_{\text{int}}}{C_{\text{sub}}}$.

The kinetic Monte Carlo model

In this section, we briefly introduce the KMC model which was used to calculate the He diffusion coefficient with vacancy-mediated mechanism. A typical approach to impurity diffusion on the FCC cation sublattice is the five-frequency model (Leclaire and Lidiard 1956). However, as will be shown in "He-vacancy interactions", the binding energies are extremely long range, comparable to the Coulombic electrostatic repulsion. Given this fact, the five-frequency model is not directly applicable. However, given the critical role typically played in impurity diffusion by the five frequencies treated in the five-frequency model, we calculated these frequencies in "Vacancy-mediated diffusion mechanism with adjusted He migration terms based on experimental Mg self-diffusion" and include them explicitly in developing the KMC model. The frequencies are ω_1 for the nearest matrix atom rotating around the solute to the adjacent vacancy, ω_2 for the exchange between the solute and the vacancy, ω_3 for the dissociating jump of the vacancy away from the solute (i.e., moving the vacancy out of the nearest neighbor position), ω_4 for the associating jump of the vacancy towards the solute into the nearest neighbor position and ω_0 for the site exchange frequency between a vacancy and a matrix atom that resides far from the substitutional solute. Each rate is determined by the formula $\omega_i = \nu^*_{\text{sub},\,i} e^{-\frac{H_i}{kT}}$, where $\nu^*_{\text{sub},i}$ is a

substitutional hop attempt frequency determined from transition state theory as described in "Diffusivity formalism".

We focus on the special treatment regarding the long-range He–V interaction, but do not present the full details of the basic KMC algorithm and the model, which can be found for instance in Refs. (Shu et al. 2013, 2015). The KMC model used in this study is based on the residence time algorithm (Bortz et al. 1975). To simulate vacancy-mediated He diffusion on the cation sublattice, an FCC rigid lattice was constructed from an $N \times N \times N$ rhombohedral crystal with periodic boundary conditions. The FCC lattice corresponds to the Mg sublattice, with no O sublattice explicitly constructed. A single vacancy and a He impurity was introduced to the cell. The vacancy migrates via thermally activated jumps which occur through nearest neighbor atom–vacancy exchanges. Due to the simplified treatment of the lattice and the lack of reliable atom–atom interactions for atoms on such a sublattice, calculating the vacancy migration barriers using the commonly used broken-bond model is challenging. Instead, we take advantage of the five migration barriers discussed above, calculated by DFT, and correct for the effect of long-range vacancy–He interaction on the activation barrier for vacancy–Mg exchange (E_0) when the vacancy is far from the He impurity. The corrected barrier E_0 can be written as

$$E_0 = E_0^{\mathrm{DFT}} + E_{\mathrm{corr}} \tag{14}$$

where E_0^{DFT} is the barrier calculated by DFT (with no He impurity explicitly considered), and E_{corr} is the correction term. Considering the initial and final position of the vacancy before and after a jump, the correction term was calculated using the final–initial-state energy (FISE) approximation

$$E_{\mathrm{corr}} = \frac{E_f - E_i}{2} \tag{15}$$

where E_i and E_f are the vacancy–He binding energies before and after the jump of the vacancy. The binding energies are taken from the $4 \times 4 \times 4$ cell DFT calculations (see Fig. 3) up to 10 Å after which they are evaluated from the Coulomb's law expression.

The size of the simulation cell, L, not only sets the true vacancy concentration, but determines the maximum range of the vacancy–He interaction. This approach is an approximation to using a very large cell with many interacting vacancies that yield the true vacancy concentration. The justification of this approximation is that, due to the strong vacancy–vacancy repulsion (see Fig. 3), the vacancies would distribute rather uniformly, typically being about L away from other vacancies. In this situation, with high vacancy concentration, the He–vacancy interaction would be always finite, and not reaching zero, which is reproduced by our approximate approach with a single He and a vacancy in a small cell.

With this method of cell size determination, the simulation time may need to be rescaled to match the experimental time. For example, for the situations with dopant–vacancy binding, an unphysically high mobile-vacancy concentration is imposed, and the simulation timescale needs to be rescaled to correct this concentration. We followed the approach proposed by Nastar and Soisson (2012) for the rescaling:

$$t = t_{\mathrm{MC}} \frac{C_V^{\mathrm{KMC}}}{C_V^{\mathrm{real}}} \tag{16}$$

where C_V^{KMC} is the vacancy concentration in the KMC simulations, and C_V^{real} is the real mobile-vacancy concentration in experiment, with dopant–vacancy binding considered.

The diffusion of He is tracked in the KMC simulations. The diffusion coefficient is then calculated by:

$$D = \frac{\langle r^2 \rangle}{6t} \tag{17}$$

where $\langle r^2 \rangle$ is the mean-square-displacement of the He atom.

Experimental details

Ion implantation and diffusion experiments

The MgO samples used in this work were from plates of synthetic MgO polished on one side, obtained from the MTI Corporation. We have two MgO samples. One MgO wafer was doped with 3000 ppm Ga^{3+} by diffusing Ga^{3+} into the MgO. The source of Ga dopant was a 1 wt% Ga bearing MgO powder, produced in a combustion synthesis using 10,000 µg/ml Ga and Mg plasma standard solutions in appropriate proportions (Chick et al. 1990). The combustion synthesis produces atomically mixed Ga-doped MgO and $MgGa_2O_4$ particles < 1 micron in diameter. This powder was fired at 1000 °C for 24 h, and then packed around the MgO wafer from MTI before being fired in air at 1500 °C for 20 days. The homogeneity of the Ga-doped MgO-wafer was verified by electron microprobe analysis. The pure MgO wafer has only minor impurities including Ca ~ 40 ppm, Al ~ 15 ppm, Si ~ 10 ppm, Fe ~ 50 ppm, Cr ~ 10 ppm, and C ~ 10 ppm, as reported by MTI.

The MgO plates were cleaved into cubes about 2 mm on a side, and mounted for ion implantation on an aluminum plate using carbon paint. The samples were implanted on polished (100) faces at room temperature, with 100 keV ^{3}He ions produced in the Extrion ion implanter at the Ion Beam Laboratory at the University at Albany. Doses were

1×10^{15} ^{3}He/cm^2. All of the samples to be implanted were mounted together on the aluminum plate and implanted simultaneously, therefore, they received the same implant dose. Following implantation, samples were stored in a desiccator until used in diffusion experiments.

For the diffusion experiments, implanted pieces of MgO were heated in crimped Pt capsules placed in 1 atmosphere Kanthal-wire wound vertical tube furnaces. Temperatures were monitored with chromel–alumel (type K) thermocouples, with uncertainties ~ 2 °C. Samples were positioned to within 5 mm of thermocouple junctions; hotspots in furnaces used for diffusion anneals were typically about 2 cm in length. Following diffusion anneals, samples were removed from capsules, cleaned briefly in ethanol, dried and placed in a desiccator until ready for ^{3}He analyses. The experiments were conducted in air, i.e., under conditions that are far more oxidizing than Earth's deep mantle. Diffusion in minerals is often sensitive to oxygen fugacity, due to the influence of internal oxidation reactions involving iron and/or other redox-sensitive cations, which control point defect concentrations. In the present experiments, our primary concern is to compare diffusion coefficients in samples with high and very low cation vacancy concentrations (using the Ga^{3+}-doped and nominally pure samples, respectively). The concentrations of redox-sensitive cations such as Fe are very low in both samples, and the difference in cation vacancy concentrations between the samples is essentially independent of oxygen fugacity.

Nuclear reaction analysis measurements

^{3}He distributions in the samples were measured with nuclear reaction analysis (NRA) using the ^{3}He(d,p)^{4}He reaction (Pronko and Pronko 1974; Trocellier et al. 2003a, b; Roselieb et al. 2006). Analyses were performed at the 4 MeV Dynamitron accelerator at the University at Albany. This nuclear reaction has been used to measure ^{3}He in a variety of minerals and ceramic materials, including zircon (Cherniak et al. 2009), zirconia (Gosset et al. 2002), britholite (Gosset and Trocellier 2005), and olivine (Cherniak and Watson 2012). The protons produced in the reaction, along with backscattered deuterons and products of various (*d, p*) and (*d*, α) reactions induced with major elements in the sample, were detected with a solid-state surface barrier detector with 1500 μm depletion depth and 100 mm^2 area positioned at 167.5° with respect to the incident beam. The beamspot incident on sample surfaces was ~ 1 to 1.5 mm on a side. A 7.5 μm thick Kapton foil was placed in front of the detector to stop some of the backscattered deuterons. Because the protons produced in the ^{3}He(d,p)^{4}He reaction are so energetic, they stand apart from other contributions to the spectrum, with very little background. The cross-section of the reaction has a maximum around 430 keV, but the peak is relatively broad (several hundred keV in width) so it is not possible to obtain high depth resolution for ^{3}He profiling using typical approaches for resonant or non-resonant NRA. For these analyses, we take the approach used in earlier studies (Cherniak and Watson 2011, 2012, 2013; Cherniak et al. 2009), performing analyses over a range of energies (0.5–0.9 MeV in this work) to better define the profile, and comparing the proton yield from the annealed sample (i.e., a sample from a diffusion experiment) to an implanted, unannealed sample at each energy step to obtain diffusivities determined by the spreading of the initial Gaussian distribution of the implanted ^{3}He.

The measured ratios of proton count yields for a sample from a diffusion experiment vs. an implanted (Costantini et al. 2002, 2003; Dieumegard et al. 1979), unannealed sample were converted into diffusivities by first evaluating the fractional loss of diffusant from an implanted profile as a function of Dt. For a semi-infinite medium with the concentration of diffusant equal to zero at $x = 0$, the distribution of the implanted species can be described as a function of depth x and time t as (Ryssel and Ruge 1986):

$$N(x,t) = \frac{N_m/2}{\sqrt{\left(1+\frac{2Dt}{\Delta R^2}\right)}}\left(\exp\left[-\frac{(x-R)^2}{2\Delta R^2+4Dt}\right]\times\left[1+\mathrm{erf}\left(\frac{\frac{R\sqrt{4Dt}}{\sqrt{2}\Delta R}+\frac{x\sqrt{2}\Delta R}{\sqrt{4Dt}}}{\sqrt{2\Delta R^2+4Dt}}\right)\right]-\exp\left[-\frac{(x+R)^2}{2\Delta R^2+4Dt}\right]\times\left[1+\mathrm{erf}\left(\frac{\frac{R\sqrt{4Dt}}{\sqrt{2}\Delta R}-\frac{x\sqrt{2}\Delta R}{\sqrt{4Dt}}}{\sqrt{2\Delta R^2+4Dt}}\right)\right]\right) \quad (18)$$

where D is the diffusion coefficient, N_m is the maximum concentration of the implanted species (in an unannealed sample), R is the range (depth in the material) of implanted species, and ΔR is the range straggle (standard deviation of the implanted distribution). Values of R and ΔR for ^{3}He from the Monte Carlo simulation program SRIM 2006 (Ziegler et al. 2006) are 3720 and 560 Å in MgO; values for N_m are ~ 0.08 at% for the implanted dose of 1×10^{15}/cm^2 for 100 keV ^{3}He.

Equation (18) describes the ^{3}He distribution, but the proton yield measured will be a function not only of the ^{3}He concentration but also of the depth in the material over which the incident deuteron beam can induce the nuclear reaction, the cross-section of the reaction as a function of energy (and depth in the material), the number of deuterons impinging on the target (N_d), and the solid angle subtended by the detector (Ω). The number of detected protons for a

profile analyzed with a given beam energy E_o can be determined from the expression

$$N_p(E_0) = N_d(E_0)\Omega \int_{x=0}^{\infty} \frac{d\sigma(E_d(x))}{d\Omega}\rho(x)dx \quad (19)$$

where $d\sigma(E_d(x))/d\Omega$ is the differential cross-section for the ^{3}He(d,p)^{4}He reaction at energy E_d, which describes the probability of the reaction occurring at this deuteron energy. The deuteron energy $E_d(x)$ will be attained at some specific depth x in the material, which is dependent on the incident deuteron energy (E_o) and the rate of energy loss for the deuterons with depth within the material. In the integral above, $\rho(x)$ represents the depth distribution of the diffusant. The above integral is evaluated numerically for each incident deuteron energy by calculating the variation of the reaction cross-section with depth in the material. Since the reaction cross-section is dependent on deuteron energy, it will vary with depth as energy is lost by incident deuterons traveling through the sample. Values of cross section as a function of energy are derived from the data of (Moller and Besenbacher 1980) and (Alimov et al. 2005) corrected for beam-detector angle. These cross-section values are then related to depth in the sample by calculating the energy loss with depth for the incident deuterons for MgO targets using stopping powers obtained from the software SRIM 2006 (Ziegler et al. 2006). The cross-section curves as a function of energy are then used to determine the proton yield from the ^{3}He concentrations $\rho(x)$ across the profile as a function of depth. The values obtained are summed to determine the proton yield for the entire profile for each incident proton energy E_o. The yields for an unannealed implanted reference sample can also be determined in this manner, and a relationship can be obtained for each incident beam energy that directly relates the ratio of proton yields for an implanted untreated sample and an annealed sample to a specific value of Dt, as outlined in previous work (Cherniak and Watson 2011, 2012). Uncertainties in diffusivities are determined from counting statistics from the detected proton signals and the variance of calculated diffusivities among incident beam energies used for each sample, which also take into consideration the uncertainties associated with stopping powers in MgO for the incident deuterons and the implanted helium.

Results and discussion

Note that in many results in this section we will include data to temperatures above the melting temperature of MgO. These values are included simply to provide a guide of trends, and represent the behavior of the metastable solid phase. They are not relevant for the stable liquid phase that would be observed above the melting temperature under equilibrium conditions.

Free vacancy and he concentrations

In this paper, we are interested in He diffusion in MgO with two impurity conditions: as-received MgO sample and Ga-doped MgO sample. The impurity content of the as-received MgO sample is given in "Ion implantation and diffusion experiments"; the Ga-doped MgO has 3000 ppm of Ga^{3+}. For the as-received sample, we need to calculate the free-vacancy concentration due to vacancy binding with multiple species of impurities. We do not include Ca contributions as it is assumed that Ca has the same valence as Mg (2+) so it will not increase the vacancy content and, furthermore, it will provide no electrostatic interaction with vacancies, and therefore, interact with them weakly. We thus included Al, Cr, Fe, Si and C. For each case, we need a vacancy–impurity binding energy to calculate the free-vacancy concentration. Because Al^{3+}, Cr^{3+} and Fe^{3+} are highly soluble in MgO (Watson and Price 2002; Van Orman et al. 2009) they have been studied extensively and we take their vacancy–impurity binding energies from the literature. These values are -0.52 eV (-50 kJ/mol) for Al^{3+}, -0.23 eV (-22 kJ/mol) for Cr^{3+} and -0.72 eV (-69 kJ/mol) for Fe^{3+} (Crispin and Van Orman 2010; Van Orman et al. 2009). As C and Si vacancy–impurity binding energies have not been measured to our knowledge, we assumed they would form tetravalent impurities and set their values to be -1.14 eV, which value was estimated as about twice the binding of a typical trivalent cation (whose value we took to be the average of Al^{3+}, Cr^{3+}, Fe^{3+} and Ga^{3+}). Then we solved for c_V^f using the equations in "Free and bound extrinsic cation vacancy concentration" with these impurity concentrations and binding energies (see Fig. 2a).

For the doped case with 3000 ppm Ga^{3+}, we expect vacancies to bind predominantly with Ga and will not consider any other impurities. Crispin and Van Orman (2010) determined the Ga–vacancy binding energy range to be between -0.60 and -1.04 eV, with an average of -0.86 eV, via impurity diffusion experiments in periclase. We solved for c_V^f using the equations in "Free and bound extrinsic cation vacancy concentration" and the 3000 ppm Ga concentration and the average -0.86 eV binding energy (see Fig. 2a).

We can see that the free-vacancy concentration ranges from about 0.1 to 1000 ppm over the temperatures and dopant levels of relevance in this study. It also converges to an asymptotic value at high temperatures, which value is the total vacancy concentration because the impurity–vacancy pairs or complexes asymptotically go to zero concentration due to entropy-driven unbinding at high temperatures.

As noted above, our approach provides enough information to estimate the He solubility, albeit with a significant

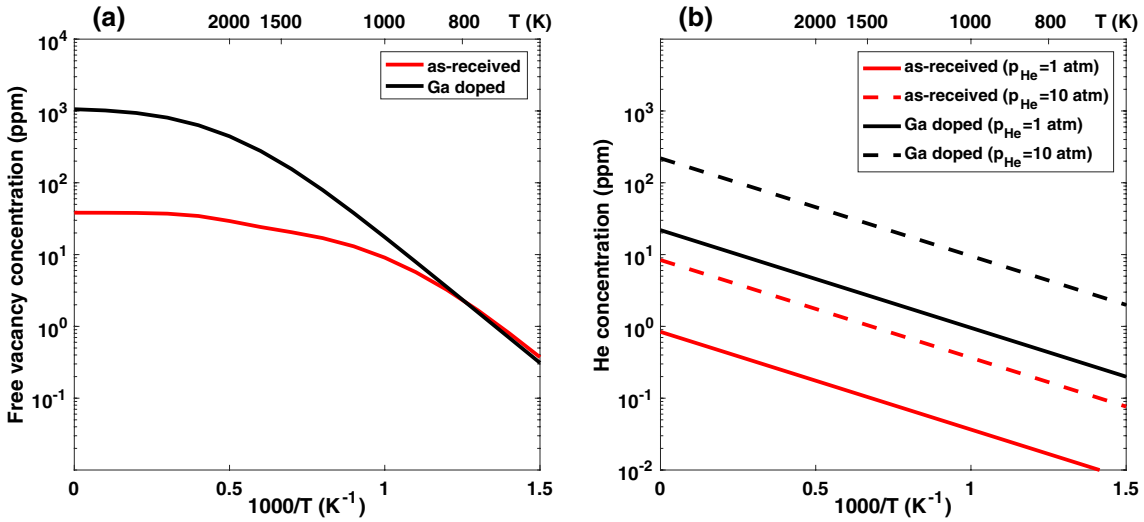

Fig. 2 **a** Free-vacancy concentration as a function of inverse temperature for the two impurity conditions of interest; **b** He concentration as a function of inverse temperature in different He gas partial pressures

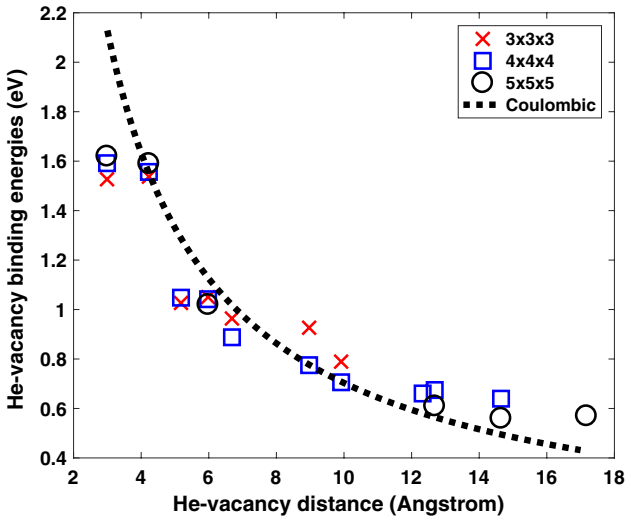

Fig. 3 DFT values of He–vacancy binding energies of different supercell sizes with the Leslie and Gillan corrections (Eq. 11) as a function of He–vacancy distances, which distances correspond to different neighbor shells. Coulombic energy of two point charges ($q = -2e$) separated in the medium of MgO is also shown, where the relative permittivity MgO is calculated from DFT to be $\varepsilon = 9.84$

uncertainty (see "Formalism for solubility of He"). To apply the equations in "Formalism for solubility of He" we need the ν_i values in Eq. (4), which were calculated in this work to be 14.38, 14.33, 14.25 THz and 15.12, 15.29, 15.34 THz for the stable site substitutional and interstitial He, respectively. The total He concentrations [as both interstitial and substitutional, determined from Eqs. (1) and (7)] for samples with different dopant content and He partial pressures as a function of temperature are shown in Fig. 2b. We note that the He concentration is lower than the total vacancy concentration for all values shown, and they do not become close until He partial pressure values approach ≈ 50 atm. In this work, we assume that the He concentration is always less than the vacancy concentration, and that we can, therefore, ignore the possibility of a given He hop being inhibited because a mediating vacancy is already filled with He.

He–vacancy interactions

As was mentioned in "He–vacancy binding energetics", finite supercell size effects are much more significant to the He–vacancy and vacancy–vacancy binding energies, due to the Coulombic interactions, than to the migration enthalpies. (Ammann et al. 2012) show that the Leslie and Gillan corrections result in good binding energy convergence with respect to the supercell size. However, as shown in Fig. 3, the He–vacancy binding energy does not converge to zero even if the distance of the two species are 17 Å apart. We also found that the Coulombic electrostatic repulsion falls almost on top of the binding energies for a wide range of separations, which indicates that the binding energies are primarily due to Coulombic interactions. The small deviations from Coulombic behavior for the farthest positions in each cell are likely due to these positions being near the middle of the cell, where the energy has to pass through a minimum and then start to increase due to the symmetry of the fields from the He and its images. In other words, these points are far enough apart that simple average Leslie and Gillan corrections begin to break down and the results are impacted by the image charges. The deviations from Coulombic behavior for very close He and vacancy are to be expected as the Coulomb interaction becomes very large and the species are very close, so significant overlap of

excess charge regionsm, deformation of charge densities, direct wave function interaction, and rehybridization can occur to reduce the Coulomb energy. The long-range interaction is treated in modeling the He diffusion using KMC, as described in "The kinetic Monte Carlo model".

DFT results of He migration terms

Interstitial mechanism

The migration path is He hopping from one interstitial site to the other neighboring interstitial site along the <001> direction and its migration barrier is 0.73 eV. We also calculated the migration barrier along the <110> direction and it is about 0.4 eV higher than the <001> direction, so the <001> direction is energetically more favorable and we do not include contributions from the <110> direction. The attempt frequency of the interstitial He is calculated following the approach in "Diffusivity formalism" and gives $\nu^*_{\text{int}} = 17.39$ THz, yielding a prefactor $D^0_{\text{int}} = 7.78 \times 10^{-7}$ m^2/s.

Vacancy-mediated diffusion mechanism with adjusted he migration terms based on experimental Mg self-diffusion

We calculate the five migration barriers corresponding to the five jump frequencies (shown in first row of Table 1, with H_i being the migration barrier for jump ω_i, $i = 0$ to 4) that will be used in the KMC simulations, as described in "Diffusivity formalism" and "The kinetic Monte Carlo model". The He position in the saddle point activated state is located at the mid-point of the He hop and the hop involves just one simple maximum for all five migrations. The attempt frequencies of all the substitutional hops (see "The kinetic Monte Carlo model") we found to be $\nu^*_{\text{sub}} = 16.07$–$17.80 \approx 17$ THz, where we use the single approximate value of 17 THz for simplicity.

Among the five hopping barriers, ω_0 is directly associated with the Mg self-diffusion migration barrier. Figure 4 shows the comparison of DFT values with previous experimental data all scaled to be consistent with a free cation vacancy concentration of $c_V = 50$ ppm.

Our raw DFT calculated Mg self-diffusivity has a migration enthalpy of $H_0 = 1.93$ eV and a prefactor of $D^0_{\text{Mg}} = 1.09 \times 10^{-6}$ m^2/s. Our predicted migration enthalpy is in reasonable agreement with previous DFT–GGA calculations, e.g., 1.90 eV (Saha et al. 2011), 2.02 eV (Ammann et al. 2012). However, our best fit to the previous experimental data (see references in the caption of Fig. 4) has a migration enthalpy of $H'_0 = 2.38$ eV and a prefactor of $D^0_{\text{Mg,exp}} = 8.12 \times 10^{-5}$ m^2/s (this fit was performed by extracting data from Arrhenius fits over experimental temperature range, with the data spaced uniformly along the $1/T$ axis, and performing a least squares fit). Written in the Arrhenius form, the DFT and experimental diffusion coefficients are

$$D_{\text{Mg}} = c_V D^0_{\text{Mg}} \exp\left[-\frac{H_0}{kT}\right] = 1.09 \times 10^{-6} c_V \exp\left[-\frac{1.93}{kT}\right] \quad (\text{m}^2/\text{s}) \tag{20}$$

$$\begin{aligned} D_{\text{Mg,exp}} &= c_V D^0_{\text{Mg,exp}} \exp\left[-\frac{H_{0,\text{exp}}}{kT}\right] \\ &= 8.12 \times 10^{-5} c_V \exp\left[-\frac{2.38}{kT}\right] \quad (\text{m}^2/\text{s}) \end{aligned} \tag{21}$$

The discrepancy between the DFT and experimental diffusion coefficients suggests that the diffusion processes associated with Mg will be more accurately treated if the DFT values are scaled to match the experimental Mg self-diffusivity. To find this scale factor, s, we divide Eq. (21) by Eq. (20), to yield

$$s = D_{\text{Mg,exp}} / D_{\text{Mg}} = 74.5 \exp\left[-\frac{0.45}{kT}\right] \quad (\text{m}^2/\text{s}) \tag{22}$$

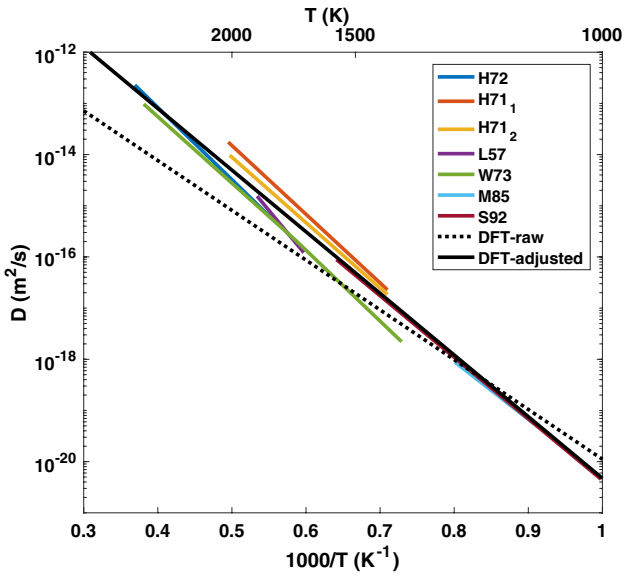

Fig. 4 DFT raw data, adjusted model and previous experimental data for Mg self-diffusion in MgO scaled to 50 ppm vacancy; previous experiments include H72 (Harding 1972), H71 (Harding et al. 1971), L57 (Parfitt and Geoffrey 1957), W73 (Wuensch et al. 1973), M85 (Martinelli et al. 1985), S92 (Sheng et al. 1992)

Table 1 DFT migration enthalpy barriers of the five hops and their adjusted values based on Mg self-diffusion experiments

	H_0	H_1	H_2	H_3	H_4
DFT barriers (eV)	1.93	0.45	0.78	1.83	2.26
Adjusted barriers (eV)	2.38	0.90	0.78	2.28	2.71

Rescaling by s changes the Mg migration barrier by $\Delta H = H_{0,\mathrm{exp}} - H_0 = 0.45$ eV. It is also reasonable to assume that other hops involving Mg might need this shift, as they are similar to Mg hops in pure MgO. We, therefore, apply this shift to all hops involving Mg. However, the hop involving He (ω_2) as well as the interstitial He hop are less likely to have the same errors. Therefore, in the absence of any information about He hop corrections, we do not correct for the He hops. The corrected migration barriers are shown in the second row of Table 1. The rescaling also changes the prefactor by $(D_{0,\mathrm{exp}}/D_0) = 74.5$. The main contribution to the prefactor for pure Mg vacancy-mediated diffusion that could contain errors is the product of the attempt frequency and the vacancy concentration $\left(\nu^* C_{\mathrm{V}}\right)$. We, therefore, assume that these factors need to be increased by $(D_{0,\mathrm{exp}}/D_0)$ in our modeling of He diffusion. Given that the attempt frequency is expected to be close to correct, we assume that this error is primarily in the mobile (free) vacancy concentration. Therefore, in the KMC modeling, we increase the vacancy concentration by the factor $(D_{0,\mathrm{exp}}/D_0)$. Following Eq. (15) this simply scales time by this same factor, which increases the overall diffusivity obtained.

He diffusion with KMC model compared to experiments

As discussed in "Free and bound extrinsic cation vacancy concentration", we consider two limiting cases, one with all vacancies being mobile and contributing to diffusion (free-vacancy case), and the other one with a portion of vacancies bound to impurities and being immobile (bound-vacancy case). With KMC simulations, we measured the He diffusion coefficient for the free-vacancy case, and then considered the dopant–vacancy binding and scaled the diffusion coefficient according to the calculated free-vacancy concentration (see "The kinetic Monte Carlo model"). Therefore, we will show the upper and lower limits for the diffusion coefficient at a given temperature. Figure 5 shows the comparison between KMC predicted diffusion coefficients (these include only vacancy mediated diffusion) and those obtained from experiments (the experimental values are also given in Table 2). Below in Fig. 6 we compare the experiments to predicted diffusion from both vacancy and interstitial mechanisms. Arrhenius fits to the experimental data of the form $D = D_0 e^{-\frac{Q}{kT}}$ yield values of $\log(D_0(\mathrm{m}^2/\mathrm{s})) = -6.7 \pm 1.0$, $Q = 0.73 \pm 0.06$ (eV) for as-received MgO and

Table 2 Experimental values for ^{3}He diffusion in MgO

Sample	T (K)	Time (s)	D (m^2 s^{-1})	log(D)	+/−
as-received (undoped)					
HeMgO-5	623	2.30×10^{6}	4.96×10^{-21}	−20.3	0.18
HeMgO-4	673	4.91×10^{5}	2.36×10^{-20}	−19.63	0.27
HeMgO-1	724	1.26×10^{4}	1.39×10^{-18}	−17.86	0.28
HeMgO-8	725	8.64×10^{4}	1.85×10^{-19}	−18.73	0.32
HeMgO-9	725	2.56×10^{5}	4.70×10^{-19}	−18.33	0.28
HeMgO-2	773	7.80×10^{3}	2.56×10^{-18}	−17.59	0.32
HeMgO-3	822	1.80×10^{3}	8.94×10^{-18}	−17.05	0.22
Ga doped					
HeGaMgO-1	726	2.76×10^{4}	5.31×10^{-19}	−18.28	0.25
HeGaMgO-2	623	1.27×10^{6}	1.27×10^{-20}	−19.90	0.19
HeGaMgO-3	773	1.44×10^{4}	2.56×10^{-18}	−17.59	0.15
HeGaMgO-4	672	3.40×10^{5}	7.31×10^{-20}	−19.13	0.13

The final column represents one standard deviation in log (D)

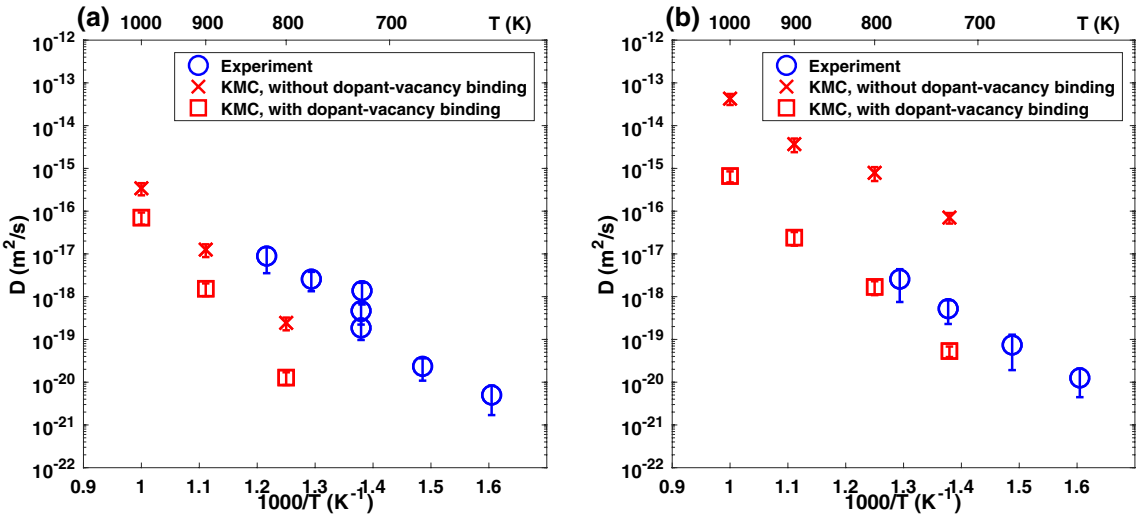

Fig. 5 He diffusivity from KMC model with and without impurity-vacancy binding effects compared with experiments. **a** is the as-received (undoped) MgO sample and **b** is the Ga-doped sample. Error bars represent one standard deviation

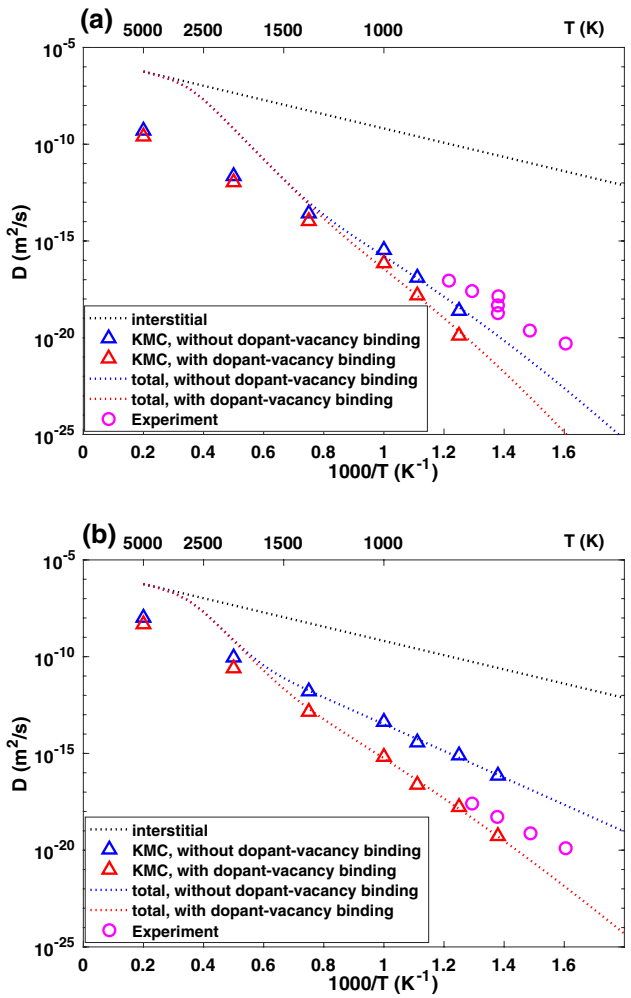

Fig. 6 He diffusivity with interstitial mechanism, vacancy-mediated mechanisms and total diffusivity with and without impurity-vacancy binding effects. **a** is the as-received MgO sample and **b** is the Ga-doped sample. The total diffusivity curves are calculated based on a fit of the KMC predicted log (D) to a second order polynomial in 1000/T. Note that the error bars of both experiments and KMC are not drawn as they are comparable or smaller than the symbols. The experimental errors can be found in Fig. 5

$\log(D_0(\mathrm{m}^2/\mathrm{s})) = -7.9 \pm 1.0, \quad Q = 0.65 \pm 0.06$ (eV) for Ga-doped MgO [uncertainties represent one standard deviation (Press 1992)]. Note that we have excluded the short-time data taken at 724 K (sample HeMgO^{-1} in Table 2) from the fitting as it appears to be outside the error bars of the other points and not to follow an otherwise consistent linear trend of all the data on the logarithmic plot (i.e., does not follow an Arrhenius behavior).

As shown in Fig. 5a, for the as-received sample, the KMC simulations underestimate the diffusion coefficients. To understand this discrepancy, one possibility is that during the process of He implantation, extra vacancies can be introduced as a result of the radiation damage. The Monte Carlo simulation program SRIM 2006 (Ziegler et al. 2006) shows that the ion implantation introduces vacancies with the peak displacement per atom (dpa) value of 13,700 ppm (the displacement energies used in SRIM are 60 and 64 eV for Mg and oxygen, respectively), which is consistent with the value of 0.014 in (Allen and Zinkle 1992).

It should be noted that SRIM calculations determine damage for implantation at 0 K; in the case of room-temperature ion implantation (as conducted in this study), a great percentage of implantation-induced damage will self-anneal during the implants, with estimates of an order of 20% of defects surviving recombination (e.g., Ziegler et al. 2006; Schut et al. 1999), which nonetheless would result in vacancy concentrations considerably higher than impurity-introduced vacancies. These additional vacancies would be mobile and contribute to He diffusion at high temperatures, before annihilating by mutual recombination with radiation induced interstitials or diffusion to a sink.

However, studies in other materials using a similar experimental and analytical approach to measure He diffusion yield results for diffusivities that are consistent with findings from modeling, as is the case for olivine (Cherniak and Watson 2012; Wang et al. 2015). This suggests that implantation-induced effects may not necessarily account for the differences between the diffusivities obtained from modeling and the experimental results for He diffusion in the undoped MgO, or that there may be a significant difference in the behavior of periclase and olivine. Such a difference may arise from the fact that, based on the present studies, periclase transports He through a vacancy mechanism, whereas He transport in olivine appears to be dominated by interstitial diffusion. This difference would make He transport in periclase much more sensitive to radiation-induced vacancies.

For the Ga-doped case, the He diffusion coefficients estimated by KMC simulations with the dopant–vacancy binding corrections agree reasonably well with the experimental results, as shown in Fig. 5b. Note that, due to the higher dopant-induced vacancy concentration, the effect of residual vacancies from He implantation would be less significant. These results suggest that the dopant–vacancy binding may have a significant influence on the number of vacancies available for diffusion, and supports the assumption of immobile dopant–vacancy complexes.

With both the interstitial diffusivity calculated in "DFT results of He migration terms" and vacancy-mediated diffusivity from KMC, we can combine the two sets of data based on Eq. (13) and obtain a final He diffusivity as shown in Fig. 6. As the KMC data does not show Arrhenius behavior [linear trend of log(D) vs. 1/T] we fit the KMC log(D) values to a second order polynomial in 1000/T.

For both with and without the dopant–vacancy binding effect, i.e., the red and blue lines in Fig. 6, D_{tot} is

approximately equal to D_{sub} (corresponding to our KMC data) at lower temperatures ($T < 1000$ K for as-received MgO sample and $T < 2000$ K for Ga-doped MgO sample, respectively). The interstitial mechanism, on the other hand, dominates the He diffusion at temperatures higher than 3000 K for the as-received and Ga-doped samples.

These trends are easy to understand qualitatively. Although the vacancy migration barrier is much higher than the interstitial migration barrier, the strong interstitial–vacancy binding energy means there are not enough interstitials to dominate the diffusion at lower temperatures. As the temperature increases, the number of interstitials also increases, and thus the effect of the low-barrier interstitial migration starts to play a role.

Conclusions

We predicted that the dominant mechanism of He diffusion in defect-bearing MgO is vacancy-mediated at lower temperatures and interstitial-mediated at higher temperatures, with a crossover between the mechanisms in the temperature range 1500–3000 K.

We found a very long tail of He–vacancy or vacancy–vacancy repulsion and this repulsion is comparable with Coulombic electrostatic repulsion. Thus, the classic five-frequency model which only treats up to the fourth nearest neighbor is not applicable in our system. Given that, we used the KMC method to model the He kinetics based on our DFT migration barriers. Because it is uncertain how impurity–vacancy binding affects He diffusion by a vacancy mechanism, we calculate lower and upper bounds for the He diffusivity, and the experimental data of the Ga-doped case lies within this range. Our model provides valuable insights on noble gas diffusion, and can be used as a foundation to explore high-pressure behavior of relevance for the deep Earth.

Acknowledgements This work is supported by the National Science Foundation under Grant No. 1265283.

References

Alimov VK, Mayer M, Roth J. 2005. Differential cross-section of the D(He-3, p)He-4 nuclear reaction and depth profiling of deuterium up to large depths. Nucl Instrum Methods Phys Res Sect B Beam Interact Mater Atoms 234:169–175

Allegre CJ, Staudacher T, Sarda P (1987) Rare-gas systematics—formation of the atmosphere, evolution and structure of the Earth's mantle. Earth Planet Sci Lett 81:127–150

Allen WR, Zinkle SJ (1992) Lattice location and clustering of helium in ceramic oxides. J Nucl Mater 191:625–629

Ammann MW, Brodholt JP, Dobson DP (2012) Diffusion of aluminium in MgO from first principles. Phys Chem Miner 39:503–514

Blochl PE (1994) Projector augmented-wave method. Phys Rev B 50:17953–17979

Bortz AB, Kalos MH, Lebowitz JL (1975) A new algorithm for Monte Carlo simulation of Ising spin systems. J Comput Phys 17:10–18

Callaway J (1974) Quantum theory of the solid state. Academic Press, New York

Cherniak DJ, Watson EB (2011) Helium diffusion in rutile and titanite, and consideration of the origin and implications of diffusional anisotropy. Chem Geol 288:149–161

Cherniak DJ, Watson EB (2012) Diffusion of helium in olivine at 1 atm and 2.7 GPa. Geochim Cosmochim Acta 84:269–279

Cherniak DJ, Watson EB (2013) Diffusion of helium in natural monazite, and preliminary results on He diffusion in synthetic light rare earth phosphates. Am Miner 98:1407–1420

Cherniak DJ, Watson EB, Thomas JB (2009) Diffusion of helium in zircon and apatite. Chem Geol 268:155–166

Chick LA, Pederson LR, Maupin GD, Bates JL, Thomas LE, Exarhos GJ (1990) Glycine nitrate combustion synthesis of oxide ceramic powders. Mater Lett 10:6–12

Costantini JM, Trocellier P, Haussy J, Grob JJ (2002) Nuclear reaction analysis of helium diffusion in britholite. Nucl Instrum Methods Phys Res Sect B Beam Interact Mater Atoms 195:400–407

Costantini JM, Grob JJ, Haussy J, Trocellier P, Trouslard P (2003) Nuclear reaction analysis of helium migration in zirconia. J Nucl Mater 321:281–287

Crispin KL, Van Orman JA (2010) Influence of the crystal field effect on chemical transport in Earth's mantle: Cr3+ and Ga3+ diffusion in periclase. Phys Earth Planet Inter 180:159–171

Dabrowski L, Szuta M (2013) Diffusion of helium in the perfect uranium and thorium dioxide single crystals. Nukleonika 58:295–300

Dieumegard D, Dubreuil D, Amsel G. (1979) Analysis and depth profiling of deuterium with the Dche-3,P)He-4 reaction by detecting the protons at backward angles. Nucl Instrum Methods 166:431–445

Fu CC, Willaime F (2005) Ab initio study of helium in alpha-Fe: dissolution, migration, and clustering with vacancies. Phys Rev B 72:064117

Gosset D, Trocellier P (2005) Determination of the helium thermal diffusion coefficient in britholite using a NRA method: new results. J Nucl Mater 336:140–144

Gosset D, Trocellier P, Serruys Y (2002) Determination of the helium diffusion coefficient in nuclear waste storage ceramics by a nuclear reaction analysis method. J Nucl Mater 303:115–124

Harding BC (1972) Diffusion of Ni and Ba in MgO up to 2500 °C. Phys Status Solidi B Basic Res 50:135

Harding BC, Price DM, Mortlock AJ (1971) Cation self-diffusion in single crystal MgO. Phil Mag 23:399

Hart SR (1984) He diffusion in olivine. Earth Planet Sci Lett 70:297–302

Henkelman G, Uberuaga BP, Jonsson H (2000) A climbing image nudged elastic band method for finding saddle points and minimum energy paths. J Chem Phys 113:9901–9904

Kresse G, Furthmuller J (1996) Efficient iterative schemes for ab initio total-energy calculations using a plane-wave basis set. Phys Rev B 54:11169–11186

Leclaire AD, Lidiard AB (1956) Correlation effects in diffusion in crystals. Phil Mag 1:518–527

Leslie M, Gillan MJ (1985) The energy and elastic dipole tensor of defects in ionic-crystals calculated by the supercell method. J Phys C Solid State Phys 18:973–982

Martinelli JR, Sonder E, Weeks RA, Zuhr RA (1985) Measurement of cation diffusion in magnesium-oxide by determining the Mg O-18 buildup produced by an electric-field. Phys Rev B 32:6756–6763

Mayeshiba T, Wu H, Angsten T, Kaczmarowski A, Song ZW, Jenness G, Xie W, Morgan D (2017) The materials simulation toolkit (MAST) for atomistic modeling of defects and diffusion. Comput Mater Sci 126:90–102

Moller W, Besenbacher F (1980) Note on the He-3 + D nuclear-reaction cross-section. Nucl Instrum Methods 168:111–114

Nastar M, Soisson F (2012) Atomistic modeling of phase transformations: point-defect concentrations and the time-scale problem. Phys Rev B 86:220102

Parfitt RL, Geoffrey D (1957) Diffusion of radioactive magnesium in magnesium oxide crystals. J Chem Phys 26:182–185

Perkins RA, Rapp RA (1973) The concentration-dependent diffusion of chromium in nickel oxide. Metall Trans 4:193–205

Press WH 1992. Numerical recipes in C: the art of scientific computing. Cambridge University Press, Cambridge, pp 662–663

Pronko PP, Pronko JG (1974) Depth profiling of He-3 and H-2 in solids using He-3(D,P)He-4 resonance. Phys Rev B 9:2870–2878

Roselieb K, Dersch O, Buttner H, Rauch F (2006) Diffusivity and solubility of He in garnet: an exploratory study using nuclear reaction analysis. Nucl Instrum Methods Phys Res Sect B Beam Interact Mater Atoms 244:412–418

Ryssel H, Ruge I (1986) Ion implantation. Wiley, New York

Saadoune I, Purton JA, de Leeuw NH (2009) He incorporation and diffusion pathways in pure and defective zircon $ZrSiO_4$: a density functional theory study. Chem Geol 258:182–196

Saha S, Bengtson A, Crispin KL, Van Orman JA, Morgan D (2011) Effects of spin transition on diffusion of Fe^{2+} in ferropericlase in earth's lower mantle. Phys Rev B 84(18):184102. https://doi.org/10.1103/PhysRevB.84.184102

Schut H, Van Veen A, Labohm F, Fedorov AV, Neeft EAC, Konings RJM (1999) Annealing behaviour of defects in helium implanted MgO. Nucl Instrum Methods Phys Res Sect B Beam Interact Mater Atoms 147:212–215

Sheng YJ, Wasserburg GJ, Hutcheon ID (1992) Self-diffusion of magnesium in spinel and in equilibrium melts—constraints on flash heating of silicates. Geochim Cosmochim Acta 56:2535–2546

Shu S, Bellon P, Averback RS. 2013. Complex nanoprecipitate structures induced by irradiation in immiscible alloy systems. Phys Rev B 87:144102

Shu S, Bellon P, Averback RS (2015) Role of point-defect sinks on irradiation-induced compositional patterning in model binary alloys. Phys Rev B 91:214107

Trocellier P, Gosset D, Simeone D, Costantini JM, Deschanels X, Roudil D, Serruys Y, Grynszpan R, Saude S, Beauvy M (2003a) Application of nuclear reaction geometry for He-3 depth profiling in nuclear ceramics. Nucl Instrum Methods Phys Res Sect B Beam Interact with Mater Atoms 206:1077–1082

Trocellier P, Gosset D, Simeone D, Costantini JM, Deschanels X, Roudil D, Serruys Y, Grynszpan R, Beauvy M (2003b) He-3 thermal diffusion coefficient measurement in crystalline ceramics by mu nra depth profiling. Nucl Instrum Methods Phys Res Sect B Beam Interact with Mater Atoms 210:507–512

Trull TW, Kurz MD (1993) Experimental measurements of He-3 and He-4 mobility in olivine and clinopyroxene at magmatic temperatures. Geochim Cosmochim Acta 57:1313–1324

Van Orman JA, Li C, Crispin KL (2009) Aluminum diffusion and Al-vacancy association in periclase. Phys Earth Planet Inter 172:34–42

vanderHilst RD, Widiyantoro S, Engdahl ER (1997) Evidence for deep mantle circulation from global tomography. Nature 386:578–584

Vineyard GH (1957) Frequency factors and isotope effects in solid state rate processes. J Phys Chem Solids 3:121–127

Wang K, Brodholt J, Lu XC (2015) Helium diffusion in olivine based on first principles calculations. Geochim Cosmochim Acta 156:145–153

Watson EB, Price JD (2002) Kinetics of the reaction MgO + $Al_2O_3 \longrightarrow MgAl_2O_4$ and Al-Mg interdiffusion in spinel at 1200 to 2000 degrees C and 1.0 to 4.0 GPa. Geochim Cosmochim Acta 66:2123–2138

Weast RC (1988) CRC handbook of chemistry and physics. CRC Press, Boca Raton

Wu H, Mayeshiba T, Morgan D (2016) High-throughput ab-initio dilute solute diffusion database. Sci Data 3:11

Wuensch BJ, Steele WC, Vasilos T (1973) Cation self-diffusion in single-crystal MgO. J Chem Phys 58:5258–5266

Zhang LQ, Van Orman JA, Lacks DJ (2009) Effective radii of noble gas atoms in silicates from first-principles molecular simulation. Am Miner 94:600–608

Ziegler J, Biersack J, Littmark U (2006) The stopping and range of ions in matter. SRIM Code